Eur. Phys. J. B **51**, 173–180 (2006)
DOI: 10.1140/epjb/e2006-00207-9

THE EUROPEAN PHYSICAL JOURNAL B

Magnetic properties and ^{119}Sn hyperfine interaction parameters of $LiMn_6Sn_6$

T. Mazet[1,a], H. Ihou-Mouko[1], J.F. Marêché[1], and B. Malaman[1]

Laboratoire de Chimie du Solide Minéral, Université Henri Poincaré-Nancy I, Associé au CNRS (UMR 7555), B.P. 239, 54506 Vandoeuvre-lès-Nancy Cedex, France

Received 15 February 2006 / Received in final form 27 March 2006
Published online 1st June 2006 –

Abstract. We have synthesized $LiMn_6Sn_6$, the first RMn_6Sn_6 compound involving an alkali metal as R element. It crystallizes in the hexagonal (P6/mmm) $HfFe_6Ge_6$-type structure. From magnetic measurements and powder neutron diffraction experiments it is found that $LiMn_6Sn_6$ magnetically orders at $T_C = 380$ K in a simple easy-plane ferromagnetic structure ($m_{Mn} = 2.58\ \mu_B$ at 2 K). The ^{119}Sn Mössbauer spectrum recorded at 5 K indicates that the tin nuclei experience huge hyperfine fields (as large as 35 T). Electronic structure calculations are used to gain information about the microscopic origin of both the hyperfine field and electric field gradient at the Sn nuclei. The former arises due to spin-dependent hybridization between the 5*s* states of Sn and the 3*d* states of Mn. The latter comes from the 5*p* charge density close to the nucleus, whose anisotropy is mainly produced through directional interactions with the 3*d* states of the first Mn neighbors. Comparison between experimental quadrupole splittings and theoretical electric field gradients allows us to propose a value of $Q = -11.2 \pm 0.7$ fm^2 for the quadrupole moment of the first excited state ($I = 3/2$) of the ^{119}Sn nucleus.

PACS. 76.80.+y Mössbauer effect; other gamma-ray spectroscopy – 71.20.Lp Intermetallic compounds – 75.25.+z Spin arrangements in magnetically ordered materials

1 Introduction

The ternary RMn_6Sn_6 intermetallics, most of them crystallizing in the pseudo-layered $HfFe_6Ge_6$-type of structure (Fig. 1), are known to be formed when R is either an alkaline-earth (R = Mg, Ca), a rare-earth (R = Y, Sc, Pr, Nd, Sm, Gd-Lu) or a transition element from Col. 4 (R = Zr, Hf) [1–5]. It has been first observed that the chemical nature of the R element strongly influences the magnetic behavior of the Mn sublattice. To summarize, when the sole Mn sublattice is ordered (i.e. when R is non-magnetic) both the magnetic order and the ordering temperature evolve with the R valency: tetravalent R (=Zr, Hf) compounds are antiferromagnets ($T_N \approx 570$ K)[4], trivalent R (=Y, Sc, Lu) compounds are helimagnets ($T_N \approx 350$ K) [2] while RMn_6Sn_6 with divalent R (=Mg, Ca, Yb) are ferromagnets ($T_C \approx 290$ K) [3,5]. In all cases, the magnetic arrangements are build upon easy-plane ferromagnetic (001) Mn layers with an almost constant saturated Mn magnetic moment of $\approx 2.2\ \mu_B$. More recently, it has been found that replacing tetravalent Sn atoms by trivalent (smaller) Ga or (larger) In atoms in the pseudo-ternaries $RMn_6Sn_{6-x}X'_x$ (R = a trivalent or a tetravalent element; X′ = Ga, In) also leads to to the stabilization of a ferromagnetic order and to an overall decrease of the ordering temperature for sufficiently high X′ contents [6–11]. Giant magnetoresistance phenomena linked to a low-field metamagnetic transition are often observed for intermediate X′ compositions [6,9]. It is conspicuous that the magnetic properties of these phases evolve with the valence electron concentration (VEC), although there is no one-to-one correspondence between VEC and magnetic behavior due to other factors such the Mn-Mn distance or the R–Mn bond [11]. This motivated us for performing other chemical substitutions, especially to study low VEC compounds. The $HfFe_6Ge_6$-type RMn_6Sn_6 compounds also present an interest for ^{119}Sn Mössbauer spectroscopy since their relatively simple unit cell comprises three crystallographically inequivalent Sn sites which are further known to experience giant hyperfine fields (up to 33 T) at their nuclei [12].

Here, we present the synthesis conditions of $LiMn_6Sn_6$, the first RMn_6Sn_6 compound involving an alkali metal as R element, and study its magnetic properties by means of magnetic measurements and powder neutron diffraction experiments. The quadrupole interactions and hyperfine fields measured by ^{119}Sn Mössbauer spectroscopy are analyzed based on scalar-relativistic full-potential L/APW+lo calculations. In a previous paper [12], we will often refer to, we have studied RMn_6Sn_6, with R = Mg, Zr and Hf, by ^{119}Sn Mössbauer spectroscopy and have used

[a] e-mail: thomas.mazet@lcsm.uhp-nancy.fr

non-relativistic muffin-tin KKR calculations to analysis the chemical bonding and the Sn hyperfine fields.

2 Experimental results and interpretation

2.1 Synthesis and crystal structure

The title compound was prepared in polycrystalline form starting from high purity (at least 99.9%) commercially available elements. As a general precaution, all sample manipulations were undertaken in a purified argon-filled glove box ensuring an oxygen level of less than 2 ppm O_2 and about 3 ppm H_2O. A pellet (≈3 g) of a stoichiometric mixture of the elements was compacted and introduced into an Mo crucible which was arc-welded. To prevent its oxidation, the Mo crucible was subsequently enclosed in a silica tube under purified argon (300 mm Hg) and then placed in a tube furnace. After a preliminary homogenization treatment of 5 days at 500 °C, the sample was tightly ground, compacted and enclosed again before a 2 weeks annealing at the same temperature. No reaction of the sample with the container material was observed. The compound is stable in air for several weeks. A room temperature X-ray diffraction pattern was obtained using a Philips X'Pert Pro diffractometer ($\lambda = 1.54056$ Å). The pattern shows that $LiMn_6Sn_6$ crystallizes in the hexagonal (P6/mmm) $HfFe_6Ge_6$-type structure (Fig. 1), although the presence of the light Li atoms cannot be checked. Tiny diffraction peaks originating from the antiferromagnetic $MnSn_2$ impurity ($T_N \approx 325$ K) [13] were also observed. A profile-matching led to the following cell parameters: $a = 5.497(1)$ Å and $c = 9.026(1)$ Å. As can be seen in Figure 2, where the cell volume of $HfFe_6Ge_6$-type RMn_6Sn_6 with non-magnetic R is plotted as a function of the metallic radius [14] of the R atom, $LiMn_6Sn_6$ presents, as $MgMn_6Sn_6$, an abnormally large cell volume. In the latter case, we ascribed [12] this anomaly to the weaker interaction of the 3*d* states of Mn with the Mg *sp* valence states compare to that occurring with the *d* valence states of a transition element R. Similar arguments are still valid when dealing with R = Li.

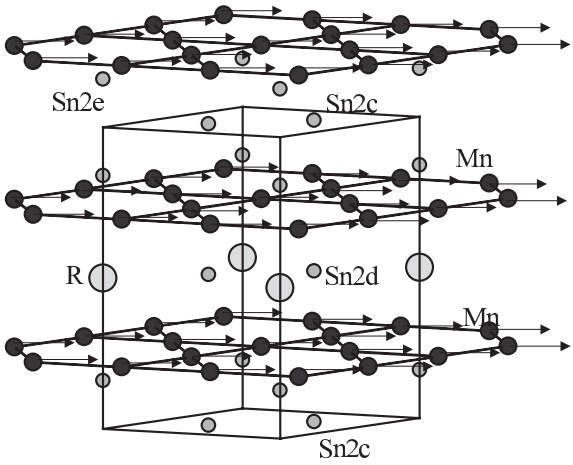

Fig. 1. Crystal and magnetic structure of $LiMn_6Sn_6$. In the $HfFe_6Ge_6$-type RMn_6Sn_6 compounds, R atoms occupy the 1*b* site (0, 0, $\frac{1}{2}$), the Mn atoms occupy the 6*i* site ($\frac{1}{2}$, 0, $z_{Mn} \approx 0.251$) and the Sn atoms occupy the 2*c*, 2*d* and 2*e* sites in ($\frac{1}{3}$, $\frac{2}{3}$, 0), ($\frac{1}{3}$, $\frac{2}{3}$, $\frac{1}{2}$) and (0, 0, $z_{Sn2e} \approx 0.180$), respectively.

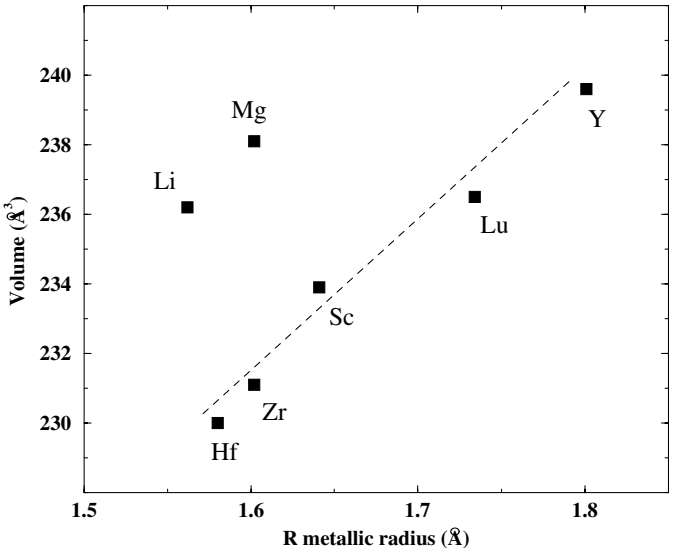

Fig. 2. Variation of the cell volume of RMn_6Sn_6 (R = Li, Mg, Sc, Y, Lu, Zr, Hf) as a function of the metallic radius of R. The dashed line is a guide for the eye.

2.2 Magnetic measurements and neutron diffraction experiments

The magnetic properties were investigated using a DSM8 MANICS magneto-susceptometer in the 5–500 K temperature range and in applied fields up to 1.5 T. Powder neutron diffraction experiments were carried out at the Institut Laue Langevin, Grenoble (France) using the D1b two-axis diffractometer ($\lambda = 2.52$ Å, step of 0.2°). Several diffraction patterns were recorded in the 2–400 K temperature range using either a standard helium cryostat ($T < 300$ K) or a furnace ($T > 300$ K). The analysis of the data was performed by Rietveld profile refinements using the software Fullprof [15]. The nuclear contribution arising from the $MnSn_2$ impurity (≈3 wt%) was taken into account during the refinements.

The thermomagnetic curve ($\mu_0 H_{appl} = 0.5$ T) recorded upon heating after zero-field cooling is shown in Figure 3. $LiMn_6Sn_6$ is characterized by a simple ferromagnetic behavior with a Curie temperature of $T_C = 380$ K. This ferromagnetic ordering temperature is significantly higher than that of RMn_6Sn_6 with divalent R ($T_C \approx 290$ K) but close to those met for certain $RMn_6Sn_{6-x}X'_x$ representatives with trivalent or tetravalent R [6,8,11]. The maximum magnetization value recorded at 5 K under an applied field of 1.5 T (inset of Fig. 3) is $M_{max.} = 12.9\,\mu_B$/f.u.

The neutron patterns recorded at 400, 300 and 2 K are depicted in Figure 4. Upon cooling below the Curie temperature no additional peak is observed, as expected for a simple ferromagnetic behavior. The strong increase of the intensity of the (002) peak indicates that the Mn

Table 1. Refined parameters of $LiMn_6Sn_6$ from neutron data at 400, 300 and 2 K.

T (K)	a (Å)	c (Å)	z_{Mn}	z_{Sn2e}	occ_{Li}	m_{Mn} (μ_B)	R_n, R_m, R_{wp}, R_e (%)
400	5.515(1)	9.060(3)	0.251(1)	0.179(1)	0.97(6)	–	3.73, ––, 8.24, 3.09
300	5.498(1)	9.027(3)	0.252(1)	0.179(1)	0.98(5)	1.76(6)	2.27, 2.86, 7.43, 3.32
2	5.491(1)	9.012(2)	0.251(1)	0.180(1)	0.98(5)	2.58(3	2.32, 2.29, 5.76, 1.75

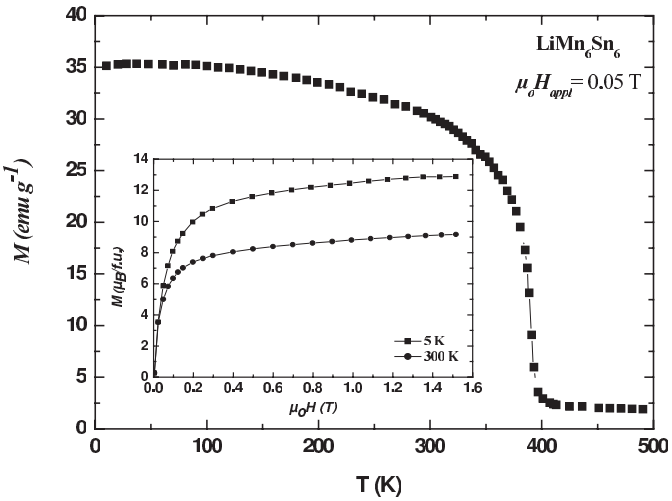

Fig. 3. Thermal variation of the magnetization of $LiMn_6Sn_6$. The inset shows the field dependence of the magnetization at 300 and 5 K.

moments markedly deviate from the c-axis. The better refinements were obtained with the Mn moments lying in the basal plane. The refined parameters as well as the main agreement factors are given in Table 1. The magnetic structure therefore consists of ferromagnetic easy-plane (001) Mn sheets ferromagnetically coupled along the c-axis (Fig. 1). This arrangement is identical to that observed for the other ferromagnetic RMn_6Sn_6 (R = Mg, Ca, Yb) [5] or $RMn_6Sn_{6-x}X'_x$ (R = Sc, Y, Lu, Zr; X′ = Ga, In) [10,11]. At 2 K, the refined Mn moment value reaches m_{Mn} = 2.58 (3) μ_B, a little higher than the ≈2.2 μ_B of the other RMn_6Sn_6. Finally, the the neutron scattering power of Li nuclei being strong enough ($b_c = -1.90$ fm), our neutron refinements, which resulted in low R_n values (2–3 %), also allow to claim that, within the error bars, the Li atoms fully occupy the 1b R site.

2.3 ^{119}Sn Mössbauer spectroscopy

The ^{119}Sn resonance absorption measurements were carried out using a constant-acceleration spectrometer. We used a $Ba^{119m}SnO_3$ source (10 mCi) kept at room temperature which also served as the reference for the isomer shifts. A polycrystalline absorber with natural abundance of the ^{119}Sn isotope and thickness of ≈15 mg/cm^2 was used. The measurement was performed at 5 K in a liquid helium cryostat. A palladium foil of 0.5 mm thickness was used as a critical absorber for tin X-ray. The spectra were fitted with a least-squares method program assuming Lorentzian peaks [17].

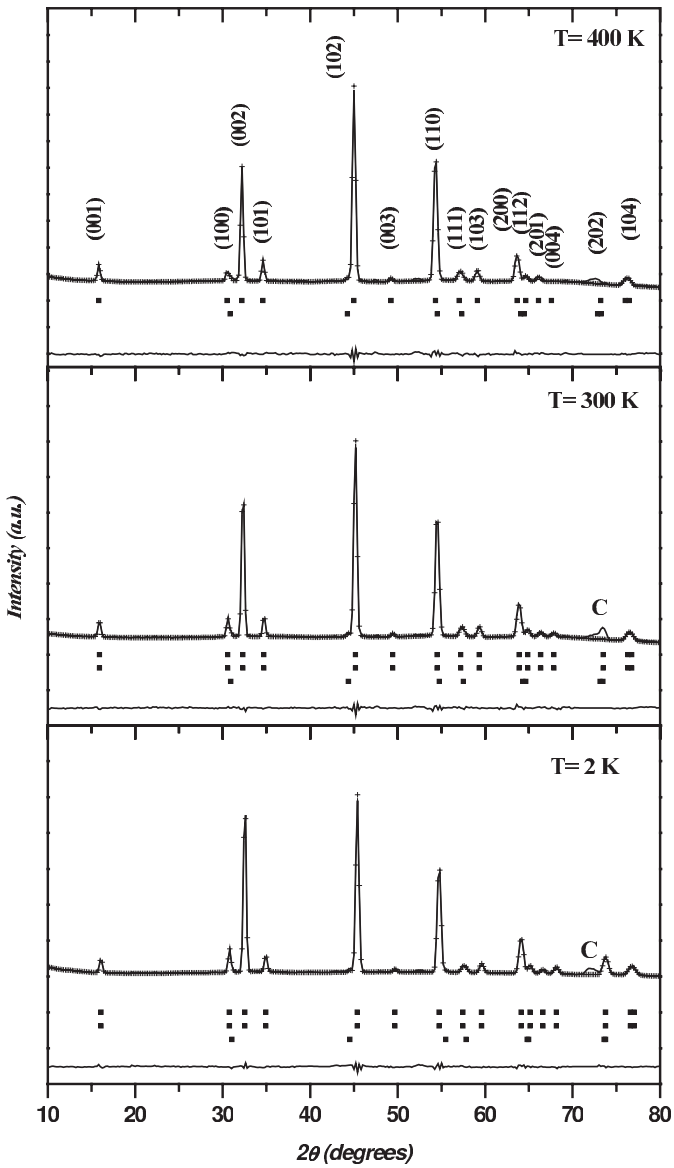

Fig. 4. Neutron diffraction patterns of $LiMn_6Sn_6$ at 400, 300 and 2 K. The lower ticks correspond to $MnSn_2$ and C points peaks arising from the tail of the cryostat.

The ^{119}Sn Mössbauer spectrum of $LiMn_6Sn_6$ at 5 K is shown in Figure 5. It is characteristic of tin nuclei experiencing very large hyperfine fields (H_{hf}) while the central peak arises from the β-Sn impurity, undetected in the diffraction patterns. Observation of the β-Sn resonance lines is due to its Lamb-Mössbauer f factor which becomes very large at low temperature [16]. The high H_{hf} values imply to consider the quadrupole interaction as a

Table 2. ^{119}Sn hyperfine interaction parameters of $LiMn_6Sn_6$ at 5 K. Estimated error bars are also indicated. The Δ values were calculated using equation (1) from the fitted 2ϵ values. For the $E_\gamma = 23.875$ keV γ transition in ^{119}Sn: 1 mm s^{-1} corresponds to $7.963(2) \times 10^{-8}$ eV or 19.253(6) MHz.

Site	Γ (mm s^{-1}) ±0.05	IS (mm s^{-1}) ±0.08	2ϵ (mm s^{-1}) ±0.06	Δ (mm s^{-1}) ±0.06	H (T) ±0.03
2*e*	1.24	2.25	+0.44	–0.88	23.6
2*d*	1.19	2.13	–0.84	+1.68	35.3
2*c*	1.15	2.23	–0.92	+1.84	30.6

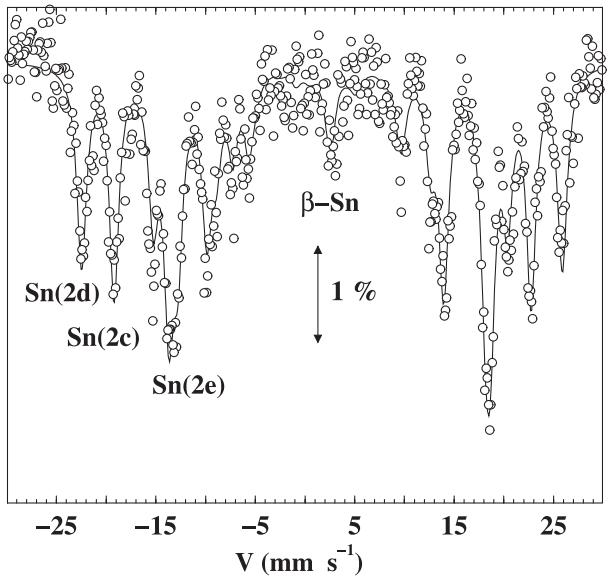

Fig. 5. ^{119}Sn Mössbauer spectrum of $LiMn_6Sn_6$ at 5 K together with its least-squares envelope.

perturbation of the magnetic hyperfine interaction. The general expression of the apparent quadrupole splitting (2ϵ) is then given to first order by:

$$2\epsilon = \Delta \left[\frac{3\cos^2\theta - 1 + \eta \sin^2\theta \cos 2\phi}{2} \right] \qquad (1)$$

where θ and ϕ are the polar and azimuthal angles of the hyperfine field direction with respect to the EFG frame of reference, respectively, while the asymmetry parameter η ($0 \leq \eta \leq 1$) and $\Delta = eQV_{zz}/2$ have the usual definitions. In $LiMn_6Sn_6$, the three Sn sites have axial symmetry, hence $\eta = 0$ and V_{zz} is directed along the *c*-axis. Further, since the Mn moments (and consequently the Sn hyperfine fields) lie in the (001) plane, $\theta = 90°$ and equation 1 simplifies to $2\epsilon = -\Delta/2$. That allows to know the sign of $\Delta = eQV_{zz}/2$ from the fitted 2ϵ values.

The spectrum has been fitted using three sextets of equal intensity, as expected from the crystal structure, while β-Sn and $MnSn_2$ (responsible for the shoulders of the central peak) were also taken into account. The resulting hyperfine interaction parameters are presented in Table 2. Using either the H_{hf} or Δ values, the sites identification is straightforward. As explained in reference [12] and also in Section 3.2, the shorter the Mn–Sn distance ($d_{Mn-Sn2d} < d_{Mn-Sn2c} < d_{Mn-Sn2e}$) the larger the H_{hf}

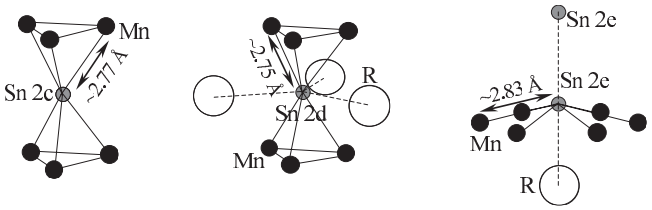

Fig. 6. Atomic environment of the inequivalent Sn sites in RMn_6Sn_6. The Mn-Sn distances are indicated.

value. On the other hand, according to the old Townes-Dailey approximation for molecules [18], often used for the interpretation of Mössbauer spectra [12,19,20], V_{zz} is proportional to $\Delta n_p = [(n_{px} + n_{py})/2 - n_{pz}]$ where n_{px}, n_{py} and n_{pz} represent the number of electrons in the p_i ($i = x, y, z$) valence orbitals (see also Sect. 3.3). From the local environment of the three Sn sites (Fig. 6) we expect: $V_{zz}^{Sn2e} > V_{zz}^{Sn2d} > V_{zz}^{Sn2c}$.

While the isomer shifts (IS), ranging between 2.13–2.25 mm s^{-1} are typical for metallic compounds, the Sn nuclei in $LiMn_6Sn_6$ experience very large hyperfine fields, similarly to previously studied RMn_6Sn_6 [12]. To our knowledge, the H_{hf} of 35.3 T we measured at the 2*d* site of $LiMn_6Sn_6$ is even the largest ever observed at Sn nuclei in Sn-based compounds. As a result of their direct neighboring environments, the Δ value for the 2*e* site significantly differs to those of the 2*c* and 2*d* sites. In all cases, the quadrupole splitting are large. In Figure 7, these values are gathered with those we published for divalent (R = Mg) and tetravalent (R = Zr, Hf) R compounds [12]. We notice an overall tendency for $|V_{zz}|$ to diminish upon increasing the R valency.

3 Band structure calculations

3.1 Computational details

The electronic structure of $LiMn_6Sn_6$ has been computed using the scalar-relativistic full-potential L/APW+lo method [21,22] as implemented in the Wien2k code [23]. We used the experimental low temperature atomic positions and cell parameters as well as non-overlapping muffin-tin spheres with radii equal to 2.60 au, 2.58 au and 2.59 au for Li, Mn and Sn atoms, respectively. The calculations have been performed using the LDA in the form given by Perdew and Wang [24]. The valence part as well as the additional local orbitals (LOs) used to describe the semicore states [25] (Li 1*s*, Mn 3*s* and 3*p*, Sn

Table 3. Theoretical and experimental values for the magnetization per formulary unit (M), the Mn magnetic moment (m_{Mn}) and the hyperfine field at the Sn nuclei (H_{hf}) in $LiMn_6Sn_6$. All the computed Sn hyperfine field values are negative with respect to the Mn moments.

	M ($\mu_B/f.u.$)	m_{Mn} (μ_B)	H_{hf}^{Sn2e} (T)	H_{hf}^{Sn2d} (T)	H_{hf}^{Sn2c} (T)
Theoretical	14.4	2.49	17.2	34.9	32.4
Experimental	12.9	2.58	23.6	35.3	30.6

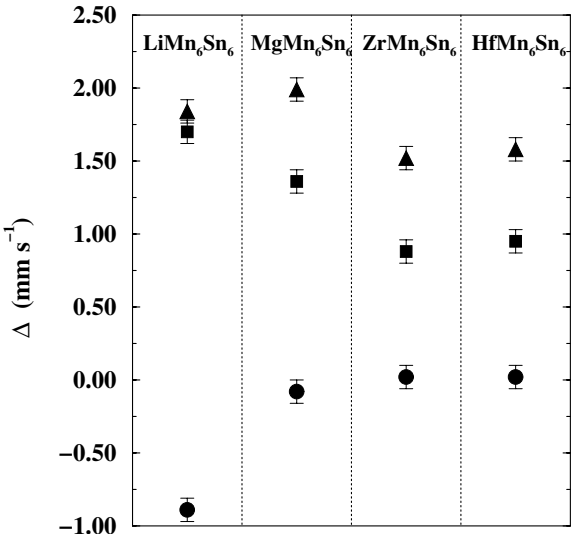

Fig. 7. $\Delta = eQV_{zz}$ /2 values at the three Sn sites of RMn_6Sn_6 with different R valency (circles: 2e site; squares: 2d site ; triangles: 2c site).

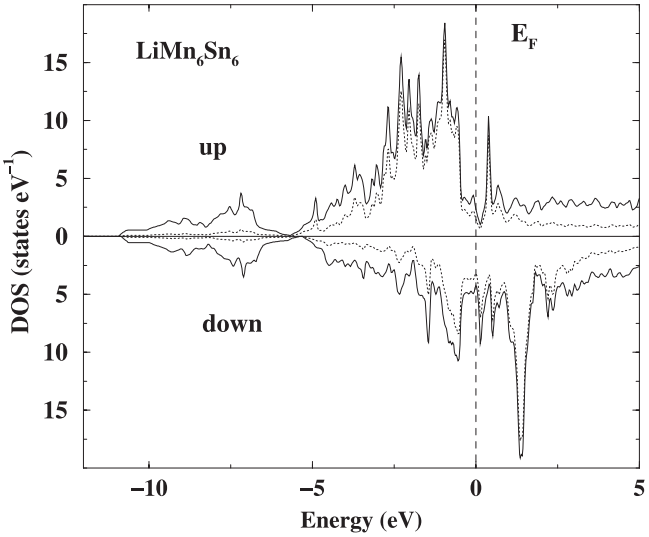

Fig. 8. Spin-polarized total (solid line) and Mn DOS (dotted line) for $LiMn_6Sn_6$. The Fermi level is marked by the dashed vertical line and is taken as the zero of the energy scale.

4d and 4p) were treated within a potential expanded into spherical harmonics up to $l = 4$. The maximum l for the valence wave functions inside the spheres was limited to $l_{max} = 10$. The wave functions in the interstitial region were expanded in plane waves with $R_{MT}K_{MAX} = 7$. The charge density was expanded up to $G_{MAX} = 14$. A mesh of 312 special k points was taken in the irreducible wedge of the Brillouin zone.

3.2 Mn magnetic moment and Sn hyperfine fields

The spin-polarized total DOS is shown in Figure 8. It is continuous over the whole energy range and is dominated by contributions from Mn atoms, except below $E \approx -6$ eV where the 5s states of Sn prevail (see Fig. 9). The magnetization of the unit cell (M) is predominantly due to the Mn magnetic moments while other atoms carry small negative hybridization induced magnetic moments. The calculated value for the magnetization M, the Mn magnetic moments m_{Mn} as well as the Fermi contact hyperfine fields (H_{hf}) at the the Sn nuclei are given in Table 3 and compared to experimental data. A good agreement between theoretical and experimental values is noticed, similarly to that we previously observed for other RMn_6Sn_6 (R = Mg, Zr, Hf) based on non-relativistic muffin-tin KKR computations [12]. Spin-polarization of the 5s states of Sn is responsible for the very large hyperfine fields at the Sn nuclei, the core polarization being negligible, as expected for

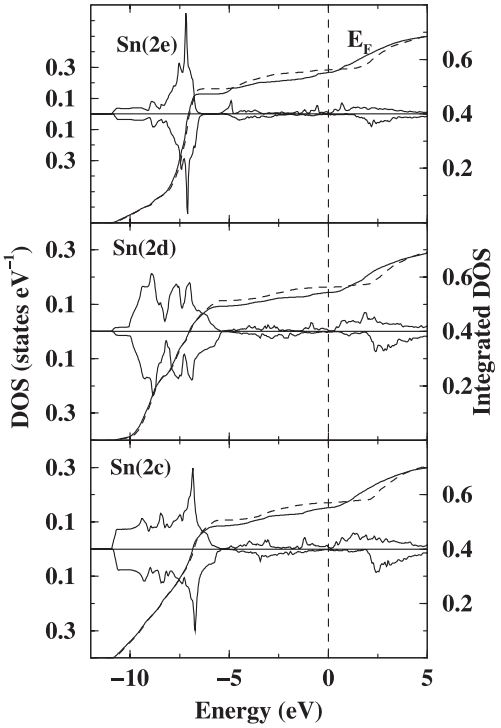

Fig. 9. Sn 5s-DOS (left scale) in $LiMn_6Sn_6$ together with the corresponding integrated 5s-DOS (right scale; solid and dashed lines correspond to spin-up and spin-down electrons, respectively). The Fermi level is marked by the dashed vertical line and is taken as the zero of the energy scale.

Table 4. Calculated $\Delta n_p(E_F)$ (Eq. (2)) and V_{zz} for the three Sn sites of $LiMn_6Sn_6$. The theoretical quadrupole splittings (Δ_{calc}), obtained using the experimental quadrupole moment value of $Q = -10.9\,\mathrm{fm}^2$ of reference [32], are compared to the experimental ones (Δ_{expt}).

Site	$\Delta n_p(E_F)$	V_{zz} (10^{21} V m^{-2})	Δ_{calc} (mm s^{-1})	Δ_{expt} (mm s^{-1})
2*e*	+0.073	+14.42	–0.99	–0.88
2*d*	–0.117	–21.92	+1.50	+1.68
2*c*	–0.125	–24.36	+1.67	+1.84

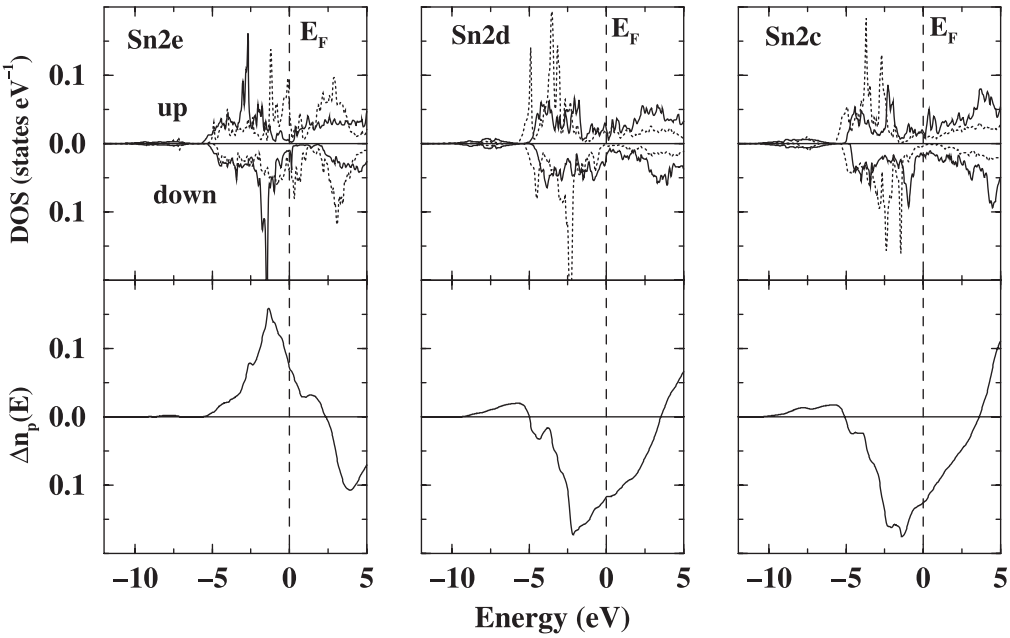

Fig. 10. $5p_x$, $5p_y$ (upper panel, solid line) and $5p_z$ (upper panel, dotted line) partial DOS at the Sn sites as well as the $5p$ anisotropy $\Delta n_p(E)$ (lower panel). The Fermi level is marked by the vertical dashed line and is taken as the zero of the energy scale.

a nominally non-magnetic element [26]. The spin-resolved 5*s*-DOS of Sn and the corresponding integrated DOS are presented in Figure 9. It can be observed that most of the *s*-polarization arises from the weakly intense part located above $E \approx -6$ eV which very likely originates from tailing of the Mn 3*d* states within the Sn spheres. In this energy range, the low energy part corresponds to the bonding states which show a preferential occupation for the minority spins while the reverse is true for the antibonding states at higher energy [12], as firstly explained by Kanamori in the case of *sp* impurities in a ferromagnetic matrix [27,28]. For the three Sn sites of $LiMn_6Sn_6$, the Fermi level falls in the energy region of negative polarization (i.e. where the minority spins dominate) leading then to negative hyperfine fields. The separation between bonding/antibonding states and consequently the 5*s* spin-polarization increase when the Mn–Sn distance decreases, hence: $H_{hf}^{Sn2d} > H_{hf}^{Sn2c} > H_{hf}^{Sn2e}$. The very good agreement we observe between experimental and calculated Fermi contact hyperfine fields suggests that the orbital and dipolar contributions to the total hyperfine field are weak (i.e. a few Teslas), especially for the 2*d* and 2*c* sites.

3.3 Electric field gradient at the Sn nuclei

The use of a potential without shape approximation allows the electric field gradient (EFG) to be calculated as described in references [29–31]. Here, because of the axial symmetry ($\eta = 0$) at the Sn sites, only the V_{zz} component is relevant. In Table 4, the computed values for V_{zz} (in 10^{21} V/m^2) are converted into ^{119}Sn Mössbauer splittings Δ_{calc} (in mm s^{-1}), using the experimental value [32] of the nuclear quadrupole constant $Q = -10.9 \pm 0.8\,\mathrm{fm}^2$, and compared with our experimental data Δ_{expt}. It can be seen that the agreement is really good. Conversely, we can use the computed V_{zz} values together with our experimental Δ values to estimate Q. Taking into account the estimated error in Δ_{expt}, our fit leads to $Q = -11.2 \pm 0.7\,\mathrm{fm}^2$. Earlier theoretical works performed on a series of non-magnetic tin compounds have led to Q values of close magnitude ($|Q| = 10.5 \pm 0.2\,\mathrm{fm}^2$ and $|Q| = 12.8 \pm 0.7\,\mathrm{fm}^2$ for the FP-LAPW [33] and FP-LMTO [34] methods, respectively), but whose sign is undetermined since the used experimental data refer to quadrupole doublets from which the sign

of Δ cannot be derived, except under special experimental conditions.

As found in other theoretical works [33,35], our computations indicate that the EFG at the Sn nuclei almost entirely arises from the asymmetry of the $5p$ charge, while d as well as semicore $4p$ contributions only play a minor role (all together no more than 3% of the total EFG). The $5p$ electrons in the near vicinity of the nucleus are obviously preponderant and we observe that more than 95% of the total EFG value is reached for electrons located at a distance not exceeding 0.12 Å from the nucleus. By integration of the $5p_x$, $5p_x$ and $5p_z$ partial DOS (Fig. 10), we calculated:

$$\Delta n_p(E_0) = \int_{-\infty}^{E_0} \frac{1}{2}[5p_x(E) + 5p_y(E)] - 5p_z(E)dE \quad (2)$$

whose sign at E_F determines that of V_{zz} as shown by previous DFT calculations [29–31]. Note that this is simply the solid state counterpart of the Townes-Dailey approximation.

Accordingly, $\Delta n_p(E_F)$ is positive for the $2e$ site whereas it is negative for the $2d$ and $2c$ sites (Tab. 4 and Fig. 10). The energy distribution of the $5p_i$ states can be understood as follows. The $5p$ states of Sn strongly hybridize with the $3d$ states of Mn [12]. The low energy ($E < E_F$) outcoming bonding states concentrate more charge on Sn atoms, since the $5p$ states of Sn lie deeper in energy than the $3d$ states of Mn, while the corresponding antibonding states, located above E_F, are mainly found on Mn atoms. For the two prismatic $2d$ and $2c$ sites (Figs. 1 and 6), the $5p_z$ states predominantly interact with the $3d$ states of their Mn axial neighbors and dominate below E_F over the $5p_x$, $5p_y$ states. The presence of three Li atoms in the direct planar environment of the $2d$ site adds small $5p_x$, $5p_y$ contributions which yield a slightly less anisotropic $5p$ shell compare to that of the $2c$ site. Conversely, for the $2e$ site these are the $5p_x$, $5p_y$ states which hybridize mainly with the $3d$ states of their nearly co-planar six Mn neighbors and dominate below E_F over the $5p_z$ states. From the plots of $\Delta n_p(E)$, the decrease of V_{zz} upon increasing the valence of R in the RMn_6Sn_6 series we noticed above (Sect. 2.3) can also be qualitatively explained. In a simple rigid band approach, it is seen that, whatever the Sn site, adding supplementary valence electrons would lead to a decrease of $\Delta n_p(E_F)$, hence to a less anisotropic $5p$ charge density.

4 Summary and concluding remarks

We have synthesized $LiMn_6Sn_6$, the first member of the RMn_6Sn_6 series involving an alkali metal as R element. This compound behaves similarly to RMn_6Sn_6 with divalent R (R = Mg, Ca, Yb) or to $RMn_6Sn_{6-x}X'_x$ (R = Sc, Y, Lu, Zr; X′ = Ga or In) with sufficiently high X′ content: it orders ferromagnetically (T_C = 380 K) and adopts a simple easy-plane ferromagnetic structure in the whole ordered temperature range. That confirms the determining influence of the valence electron concentration upon the magnetic properties of the Mn sublattice within this family of compounds. The huge hyperfine fields and the quadrupole interactions measured by ^{119}Sn Mössbauer spectroscopy experiments have been analyzed based on FP-L/APW+lo electronic structure calculations. The Sn hyperfine fields mainly arise from the Fermi contact interaction with the $5s$ states of Sn which are spin-polarized through hybridization with the magnetic $3d$ states of neighborings Mn atoms. The EFG existing at the Sn nuclei is almost entirely due to the anisotropy of the $5p$ electrons close to the nucleus. When compared to the experimental quadrupole interactions, the calculated EFG allow to derive a value of $Q = -11.2 \pm 0.7\,\mathrm{fm}^2$ for the ^{119}Sn first excited state quadrupole moment. Band structure calculations are a reliable tool for analyzing hyperfine interactions by allowing a microscopic understanding of experimental facts often difficult to fully interpret. It would now be interesting to extend the study to $RMn_6Sn_{6-x}X'_x$ (X′ = Ga or In) solid solutions involving monovalent (R = Li) or divalent (R = Mg, Ca, Yb) R element, for a better understanding of the role of the various possible kinds of exchange interaction operative in these systems. In such complex ternary and pseudo-ternary intermetallics, direct exchange, RKKY-type indirect exchange and even superexchange (through non-magnetic Sn/X′ or R connecting atoms) Mn–Mn interactions are likely involved. Synthesis are in progress.

C. Herold and N. Emery (LCSM) are warmly acknowledged for providing us shiny Li metal. We are indebted to the Institut Laue Langevin of Grenoble (France) for the provision of research facilities. We also thank our local contact (Olivier Isnard) for his kind help during the neutron diffraction measurements.

References

1. B. Malaman, G. Venturini, B. Roques, Mat. Res. Bull. **23**, 1629 (1988)
2. G. Venturini, D. Fruchart, B. Malaman, J. Alloys Compd. **236**, 102 (1996)
3. T. Mazet, G. Venturini, R. Welter, B. Malaman, J. Alloys Compd. **264**, 71 (1998)
4. T. Mazet, R. Welter, B. Malaman, J. Alloys Compd. **284**, 54 (1999)
5. T. Mazet, R. Welter, B. Malaman, J. Magn. Magn. Mater. **204**, 11 (1999)
6. S. Zhang, P. Zhao, Z. Cheng, R. Li, J. Sun, H. Zhang, B. Shen, Phys. Rev. B **64**, 212404 (2001)
7. C. Lefevre, G. Venturini, A. Vernière, B. Malaman, J. Alloys Compd. **334**, 53 (2002)
8. C. Lefevre, G. Venturini, A. Vernière, B. Malaman, J. Alloys Compd. **345**, 36 (2002)
9. F. Canepa, M. Napoletano, C. Lefevre, G. Venturini, J. Alloys Compd. **349**, 6 (2003)
10. C. Lefèvre, A. Vernière, G. Venturini, B. Malaman, J. Alloys Compd. **361**, 40 (2003)
11. T. Mazet, O. Isnard, B. Malaman, J. Phys.: Condens. Matter **17**, 1547 (2005)
12. T. Mazet, J. Tobola, G. Venturini, B. Malaman, Phys. Rev. B **65**, 104406 (2002)

13. G. Le Caer, B. Malaman, G. Venturini, I.B. Kim, Phys. Rev. B **26**, 5085 (1982)
14. E. Teatum, K. Gschneidner, J. Waber, LA-2345, US department of Commerce, Washington DC, (1960); see also, W.B. Pearson, *The Crystal Chemistry and Physics of Metals and alloys* (Wiley-Interscience, New-York, 1972)
15. J. Rodriguez-Carvajal, Physica B **192**, 55 (1993)
16. C. Hohenemser, Phys. Rev. **139**, A185 (1965)
17. G. Le Caër, private communication
18. C.H. Townes, B.P. Dayley, J. Chem. Phys. **17**, 782 (1949)
19. J.M. Friedt, J.P. Sanchez, G.K. Shenoy, J. Chem. Phys. **65**, 5093 (1976)
20. J.P. Sanchez, J.M. Friedt, B. Djermouni, G. Jehanno, J. Phys. Chem. Solids **40**, 585 (1979)
21. D.J. Singh, *Planewaves, Pseudopotentials and the LAPW method* (Kluwer, Dordrecht, 1994)
22. E. Sjöstedt, L. Nordström, D.J. Singh, Solid State Comm. **114**, 15 (2000)
23. P. Blaha, K. Schwarz, G.K.H. Madsen, D. Kvasnicka, J. Luiz, *Wien2k, An Augmented Plane Wave + Local Orbitals Program for Calculating Crystal Properties* (Karlheinz Schwarz, Tech. Univ. Vienna, Austria); improved and updated version of P. Blaha, K. Schwarz, P. Sorantin, S.B. Trickey, Comput. Phys. Commun. **59**, 339 (1990); see also K. Schwarz, P. Blaha, G.H.K. Madsen, Comput. Phys. Commun. **147**, 71 (2002), in this work, version 2k.03 was used
24. J.P. Perdew, Y. Wang, Phys. Rev. B **45**, 13244 (1992)
25. D. Singh, Phys. Rev. B **43**, 6388 (1991)
26. H. Akai, M. Akai, S. Blügel, B. Drittler, H. Ebert, K. Terakura, R. Zeller, P.H. Dederichs, Suppl. Prog. Theor. Phys. **101**, 11 (1990)
27. J. Kanamori, H. Katayama-Yoshida, K. Terakura, Hyperfine Interact. **8**, 573 (1981)
28. J. Kanamori, H. Katayama-Yoshida, K. Terakura, Hyperfine Interact. **9**, 363 (1981)
29. P. Blaha, K. Schwarz, P. Herzig, Phys. Rev. Lett. **54**, 1192 (1985)
30. P. Blaha, K. Schwarz, P.H. Dederichs, Phys. Rev. B **37**, 2792 (1988)
31. K. Schwarz, C. Ambrosch-Draxl, P. Blaha, Phys. Rev. B **42**, 2051 (1990)
32. H. Haas, M. Menningen, H. Andreasen, S. Damgaard, H. Grann, F.T. Pedersen, J.W. Petersen, G. Weyer, Hyperfine Interact. **15/16**, 215 (1985)
33. P.E. Lippens, J. Olivier-Fourcade, J.C. Jumas, Hyperfine Interact. **126**, 137 (2000)
34. A. Svane, N.E. Christensen, C.O. Rodriguez, M. Methfessel, Phys. Rev. B **55**, 12572 (1997)
35. S. Jalali Asadabadi, S. Cottenier, H. Akbarzadeh, R. Saki, M. Rots, Phys. Rev. B **66**, 195103 (2002)